Arch. Metall. Mater. **71** (2026), 2, 667-675

DOI: https://doi.org/10.24425/amm.2026.158859

YONG CHEN[1,2*], YEFANG WANG[1,2], TAO ZHANG[1,2], WANGWANG YU[1,2]

COMPARATIVE STUDY ON WELDING EFFICIENCY, MACROSTRUCTURAL/MICROSTRUCTURAL CHARACTERISTICS, AND MECHANICAL PROPERTIES FOR SEVEN-WIRE ROTATING ARC ELECTROGAS WELDING AND SINGLE-WIRE ELECTROGAS WELDING

This study comparatively evaluates the welding efficiency, macrostructural/microstructural characteristics, and mechanical properties of welded joints for seven-wire rotating arc (SRA) electrogas welding (EGW) and single-wire EGW under identical welding parameters. The results demonstrate that SRA EGW achieves superior performance over single-wire EGW in multiple critical aspects: the average welding speed, wire melting rate, and resistance heat of wire extension are increased by approximately 20%, 4%, and 38%, respectively. From a macrostructural perspective, SRA EGW joints exhibit enhanced sidewall penetration. Microstructurally, both the weld zone (WZ) and heat-affected zone (HAZ) of SRA EGW are characterized by finer grain sizes; notably, despite both welding processes yielding relatively fine microstructures, SRA EGW welds contain a higher proportion of acicular ferrite (AF) compared to single-wire EGW counterparts. These structural advantages directly contribute to improved mechanical properties: the average tensile strength of SRA EGW joints reaches 561 MPa (versus 540 MPa for single-wire EGW), with the WZ tensile strength measuring 600 MPa (versus 589 MPa for single-wire EGW); meanwhile, the average impact energy of SRA EGW welds is 78 J, surpassing the 72 J observed for single-wire EGW welds.

Keywords: Electrogas welding; seven-wire rotating arc; welding efficiency; microstructure; mechanical properties

1. Introduction

In the welding industry, welding wire serves as one of the core materials in the welding process, and its type, specification, and application method directly influence welding quality, efficiency, and cost [1,2]. Traditional single-wire electrogas welding (EGW) is extensively employed across various welding applications [3], primarily owing to its operational simplicity and broad adaptability [4,5]. Nevertheless, with the continuous improvement requirements in welding efficiency and quality, research scholars have started to explore more high-performance welding technologies. As an innovative welding material, the seven-wire rotating arc (SRA) welding wire has gradually emerged as a research focus in the welding field, attributed to its unique structural innovations and superior welding performance [6].

The SRA welding wire is constructed by rotating and twisting seven fine wires into an integrated structure [7]. During the welding process, the rotating arc not only effectively expands the arc's scanning range but also enhances the stirring effect on the molten pool. This unique structural advantage optimizes the weld formation quality while significantly improving both the stability of the welding process and the arc's penetration capability. Its performance is particularly notable in the single-pass welding of thick plates, where it demonstrates strong adaptability to such demanding application scenarios. Compared with traditional single-wire, the SRA welding wire exhibits superior performance in two key aspects: the uniformity of energy distribution in the welding zone and the precision of heat input control. Collectively, these merits provide a novel technological approach for achieving efficient and high-quality welding in industrial applications.

Fang et al. carried out a study on SRA submerged arc welding (SAW), in which they compared Φ4.0 mm SRA SAW with Φ4.0 mm single-wire SAW. Specifically, they investigated how electromagnetic pressure, resistance heat from wire extension, and the rotating arc influence the process performance and microstructure of SRA SAW [8]. The results revealed that the dilution rate of both SRA SAW and single-wire SAW increased with rising welding current. Under identical welding conditions,

---

[1] NANJING UNIVERSITY OF INDUSTRY TECHNOLOGY, INDUSTRIAL PERCEPTION AND INTELLIGENT MANUFACTURING EQUIPMENT ENGINEERING RESEARCH CENTER OF JIANGSU PROVINCE, NO. 1 YANGSHAN NORTH ROAD, NANJING 210023, CHINA
[2] NANJING UNIVERSITY OF INDUSTRY TECHNOLOGY, COLLEGE OF MECHANICAL ENGINEERING, NO. 1 YANGSHAN NORTH ROAD, NANJING 210023, CHINA

* Corresponding author:

the dilution rate of SRA SAW was approximately 33% lower than that of single-wire SAW; additionally, the deposition rate of SRA SAW was roughly 40% higher in comparison.

Wang et al. leveraged the flexible assembly feature of SRA welding wires to study Fe-Cu-Ni-Mo-Ti high-entropy alloy (HEA) coatings and their in-situ synthesized carbide-reinforced HEA counterparts [9]. These coatings were prepared via gas tungsten arc welding (GTAW) cladding using FeCuNiMoTi and FeCuNiMoTiC SRA welding wires, respectively. The results demonstrated that both types of coatings consist of BCC phase (as the major phase) and FCC phase (as the minor phase). Notably, the addition of carbon fiber enabled the in-situ formation of carbide reinforcement phases in the Fe-Cu-Ni-Mo-Ti-C HEA coating, which significantly enhanced the coating's hardness and improved its wear resistance.

Yang et al. explored the effects of polarity and shielding gases on droplet transfer behavior and weld formation trends in SRA gas metal arc welding (GMAW) under consistent welding parameters [10]. Their findings showed that arc shapes varied with polarity even when using the same shielding gas: in direct current electrode positive (DCEP) mode, both arc length and width were smaller than those in direct current electrode negative (DCEN) mode. For a given polarity with different shielding gases, arc length and width decreased gradually as the CO_2 content in the shielding gas increased. In DCEP mode, droplet transfer was characterized by both globular and projected modes. While droplet transfer modes differed between polarities under varying shielding gas conditions, they remained essentially consistent for the same polarity. Moreover, as CO_2 content increased, weld bead formation improved progressively.

Xu et al. employed SRA welding wires to investigate the process characteristics of laser-metal inert gas (MIG) hybrid welding for 5A06 aluminum alloy [11]. The results indicated that the influence of key welding parameters on weld formation was consistent with that observed in conventional wire laser-arc hybrid welding. The introduction of a high-energy-density laser heat source further accentuated the advantages of the self-rotation property of SRA welding wires. Specifically, when the welding current ranged from 130 to 200 A, an increase in current led to a higher rotation frequency of the SRA welding wire – this amplified the benefits of the rotation property, including expanded weld width and effective inhibition of welding porosity.

Chen et al. conducted in-depth research on SRA EGW, focusing primarily on droplet transfer characteristics [12], arc rotation coupling behaviors [13], and the temperature field and flow field of the molten pool during welding [14]. The results showed that during the SRA EGW process, the coupled motion of arc rotation can be decoupled into three components: axial motion, coupled motion, and circumferential rotation motion. When the welding torch did not swing along the plate thickness direction, the SRA exhibited a spiral climbing motion; in contrast, when the torch swung along the plate thickness direction, the SRA displayed a reciprocating spiral climbing motion.

This paper aims to conduct a comparative analysis of the performance differences between SRA EGW and single-wire EGW, evaluating the respective advantages and disadvantages, and exploring the potential of seven-wire in industrial applications. Through experimental research and data analysis, this study provides a theoretical foundation and practical reference for the selection of welding filler materials, contributing to the advancement and innovation of welding industry technologies.

2. Experimental materials, methods, and equipment

Figs. 1(a) and 1(b) illustrate the top-view and back-view morphologies of the arc and molten pool captured during the EGW process, respectively. The base metal (BM) utilized is AH36 low-alloy high-strength steel, which is currently widely adopted in shipyards for welding the vertical seams of large closure structures. Its chemical composition and mechanical properties are summarized in TABLES 1 and 2, respectively. The butt-joint test plates employed had dimensions of 500 mm × 200 mm × 20 mm, with a V-shaped groove featuring a 20° single-sided groove angle and a 5 mm root gap. A schematic diagram of the butt-joint test plate is provided in Fig. 1(c).

The filler metal consisted of a 1.6 mm-diameter seven-wire, which was formed by rotating and twisting seven 0.53 mm-diameter fine welding wires. For comparison, a conventional 1.6 mm-diameter single-wire was also used. All the aforemen-

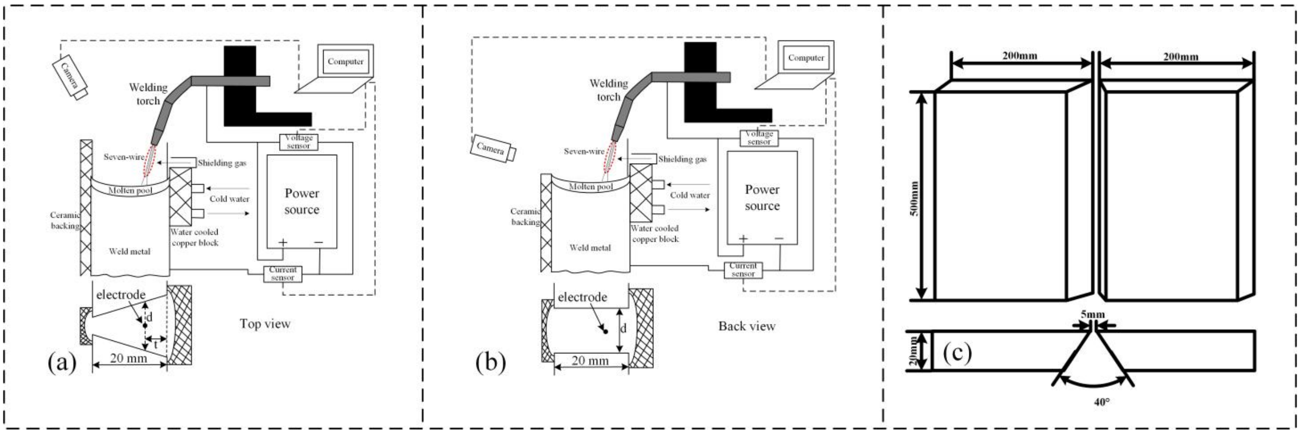

Fig. 1. Schematic diagram of welding equipment and butt-joint test plate [7]: (a) Top view, (b) Back view, (c) diagram of the butt-joint test plate

TABLE 1

Chemical composition of AH36 and ER50-G (wt.%)

Materials	**C**	**Si**	**Mn**	**P**	**S**	**Cu**	**V**	**Cr**	**Ni**	**Mo**
AH36	≤0.18	0.10-0.50	0.7-0.16	≤0.035	≤0.035	≤0.35	0.03-0.10	≤0.20	≤0.40	≤0.08
ER50-G	0.075	0.17	1.49	0.008	0.006	0.21	—	—	—	0.32

TABLE 2

Mechanical properties of AH36 and ER50-G

Material	**Yield strength (MPa)**	**Tensile strength (MPa)**	**Elongation (%)**	**Impact absorbed energy (J)**	
AH36	≥355	490~620	≥21	Longitudinal	Transverse
				≥34 (0°C)	≥24 (0°C)
ER50-G	≥420	≥500	≥22	≥27(-30°C)	

tioned welding wires conformed to the GB/T ER50-G grade, and their chemical composition and mechanical properties are listed in TABLES 1 and 2.

To conduct a comprehensive comparison between SRA EGW and single-wire EGW, experiments were carried out under identical welding conditions.

Before welding, the surface of the test plate and both sides of the groove were cleaned using a grinding machine. Subsequently, alcohol was applied to remove oil, rust, and other impurities, and the test plate was weighed with an electronic balance prior to the welding process.

For the welded joint specimens, water grinding was first performed, followed by polishing with 3.5 μm diamond polishing paste. After polishing, the specimens were etched using a 5% nitric acid-alcohol solution, then cleaned with alcohol and dried with hot air. The prepared metallographic samples were observed under an optical microscope (Leica MM6) for microstructural analysis. Further microstructural observation of the welded joints was conducted using a tungsten filament scanning electron microscope (SEM, Model JSM-8680, manufactured by JEOL). Vickers hardness testing was carried out 3 times with a test load of 10 kg and a dwell time of 15 seconds. The hardness test points were mainly distributed in the heat-affected zone (HAZ), fusion line (FL), and BM region. In accordance with the Rules for Materials and Welding of the China Classification Society (CCS), the mechanical properties of the welded joints were primarily evaluated through tensile tests (both longitudinal and transverse), bending tests (side bend), and impact tests. The specimens for these mechanical property tests were cut from the butt-welded test plates, and a schematic diagram of the welded joint mechanical property specimens for EGW is presented in Fig. 2.

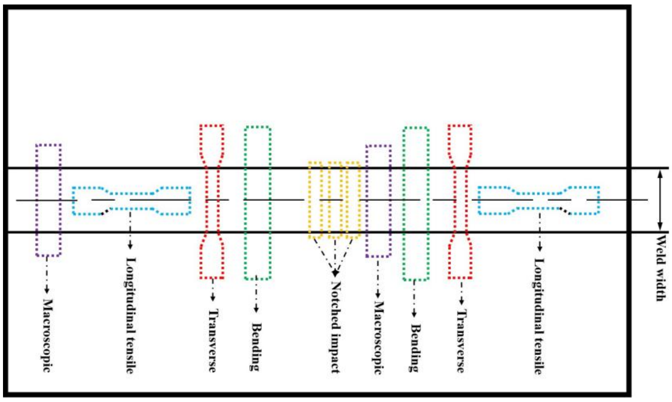

Fig. 2. Schematic diagram of mechanical properties specimens of butt joint in EGW

3. Results and discussion

3.1. Welding efficiency of SRA EGW and single-wire EGW

The welding speed, filler metal deposition rate, and wire melting rate of SRA EGW and single-wire EGW were measured under identical welding conditions (detailed in TABLE 3). The welding current is 335 A, the welding voltage is 35 V, the shielding gas is 80%Ar + 20%CO_2, the gas flow rate is 30 L/min, and the contact tip to workpiece distance (CTWD) is 40 mm. These welding parameters are the welding parameters that two types of welding wires can achieve stable welding in the EGW process. To ensure result accuracy, three replicate measurements were conducted for each parameter; the average values were calculated and are presented in Fig. 3. As shown in Fig. 3, both EGW processes achieved high deposition efficiency. This is primarily attributed to the confined environment of the EGW process, where most spatter is trapped by the groove sidewalls and falls back into the molten pool. Additionally, both processes use solid welding wires, which generate minimal slag. Notably, compared with single-wire EGW, the SRA EGW process exhibited higher average welding speed, filler metal deposition rate, and wire melting rate – with respective improvements of approximately 20%, 7%, and 4%.

Theoretical analysis indicates that the energy required to melt the welding wire primarily consists of two components: arc heat generated in the anode region and resistance heat produced by wire extension. Given that the voltage drop in the anode region is extremely small and can be effectively neglected, the difference in arc heat between the two EGW processes is also insignificant. Consequently, the primary factor contributing to the disparity in wire melting rates between the two processes is the resistance heat from wire extension. This section therefore aims to quantify the difference in resistance heat from the perspective of wire extension, and further explore the underlying mechanisms responsible for the varying wire melting rates of the two EGW processes.

TABLE 3

Welding parameters of SRA EGW and single-wire EGW

EGW technologies	SRA EGW	Single-wire EGW
Position of wire	1/3 plate thickness to the front weld seam	
Welding torch swing (mm)	0	
Welding current (A)	335	
Welding voltage (V)	35.5	
Shielding gas	80%Ar + 20%CO_2	
Gas flow rate (L/min)	30	
CTWD (mm)	40	

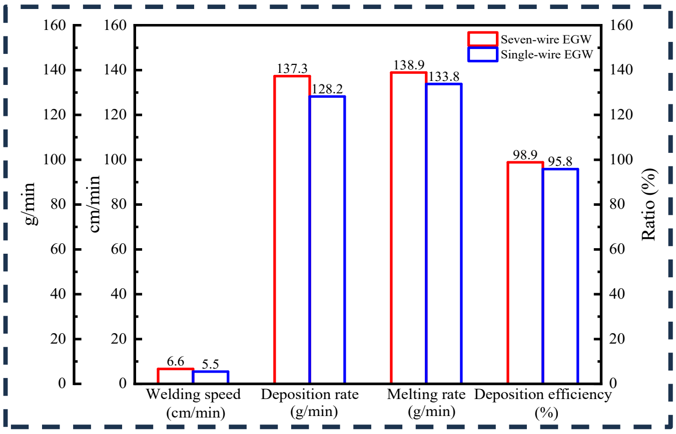

Fig. 3. The measurement results of welding speed, deposition rate, melting rate and deposition efficiency between SRA EGW and single-wire EGW

Figs. 4(a) and 4(b) show the arc shapes of the two EGW processes under the same welding conditions (as specified in Fig. 3). Measurements indicate that the arc length of SRA EGW is shorter than that of single-wire EGW. Given that the CTWD is identical for both processes, the wire extension in SRA EGW is longer than that in single-wire EGW.

Additionally, although the two types of welding wires have the same outer diameter, their distinct structures result in different cross-sectional areas. Fig. 4(c) illustrates the cross-sectional areas of the two wires: the dashed line denotes the outer diameter of the single wire, while the seven solid circles represent the seven individual fine wires that constitute the seven-wire.

As shown in Fig. 4(c), for the seven-wire, the conductive cross-sectional area refers to the sum of the cross-sectional areas of its seven individual fine wires; for the single-wire, by contrast, the conductive cross-sectional area corresponds to the total cross-sectional area of the outer dashed circle (as indicated in the figure). To quantitatively compare the resistance heat generated in the two EGW processes under identical welding conditions, the conductive cross-sectional areas of the two wires are respectively expressed by Eqs. (1) and (2) [12]:

$$S_d = \pi \left(\frac{D}{2} \right)^2 \tag{1}$$

$$S_q = 7\pi \left(\frac{D}{6} \right)^2 \tag{2}$$

In the equations, S_d represents the cross-sectional area of the single-wire, S_q represents the cross-sectional area of the seven-wire, D denotes the outer diameter of the two welding wires. The resistance heat for the two EGW processes can be expressed by Eqs. (3) and (4), respectively:

$$Q_d = \frac{\rho_d L_{ed} I^2}{S_d} \tag{3}$$

$$Q_q = \frac{\rho_q L_{eq} I^2}{S_q} \tag{4}$$

In the equations, Q_d represents the wire extension resistance heat (W) for the single-wire EGW, and Q_q represents the wire extension resistance heat (W) for the seven-wire EGW, ρ_d, ρ_q are the resistivities of the wire extension ends of the single-wire and seven-wire, respectively (π·mm), L_{ed}, L_{eq} represent the wire extension lengths of the single-wire and seven-wire, respectively

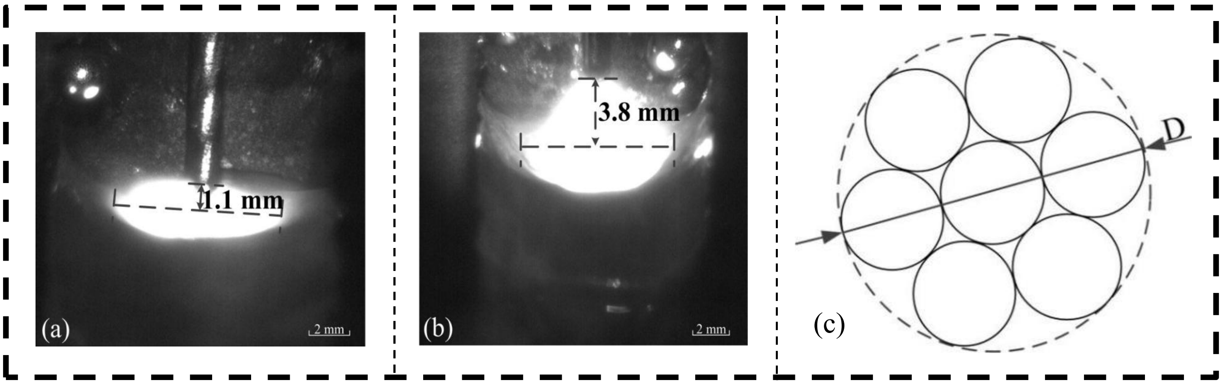

Fig. 4. Comparison of arc length and cross-sectional area between two EGW welding processes: (a) SRA EGW arc length, (b) Single-wire EGW arc length, (c) Schematic diagram of cross-sectional area of two types of welding wires

(mm). By substituting equations (1) and (2) into Eqs. (3) and (4), the results are shown in Eqs. (5) and (6):

$$Q_d = \frac{4\rho_d L_{ed} I^2}{\pi D^2} \tag{5}$$

$$Q_q = \frac{36\rho_q L_{eq} I^2}{7\pi D^2} \tag{6}$$

Assuming that the resistivities at the wire extension ends of both welding wires are the same, the ratio of the wire extension resistance heat of the SRA EGW to that of the single-wire EGW can be expressed as:

$$\eta_Q = \frac{9L_{eq}}{7L_{ed}} \tag{7}$$

From Eq. (7), it can be observed that under identical welding conditions, the ratio of the wire extension resistance heat generated in SRA EGW to that in single-wire EGW is directly proportional to the wire extension length of the seven-wire and inversely proportional to that of the single-wire. As previously noted, the CTWD is the same for both EGW processes. Arc shape analysis reveals that the arc length for SRA EGW (L_{eq}) is 1.1 mm, whereas that for single-wire EGW (L_{ed}) is 3.8 mm. According to TABLE 3, the CTWD for both processes is 40 mm. Consequently, the wire extension length of the seven-wire (L_{eq}) is 38.9 mm, and that of the single wire (L_{ed}) is 36.2 mm. Substituting these values into Eq. (7) yields a ratio of 1.38 for the wire extension resistance heat generated in SRA EGW compared to single-wire EGW. In other words, under the same welding conditions, the wire extension resistance heat generated in SRA EGW is 38% higher than that in single-wire EGW.

Thus, the higher wire melting rate in SRA EGW compared to single-wire EGW can be attributed to its greater resistance heat. Additionally, the relatively enclosed environment of both EGW processes causes most generated spatter to be retained on the groove sidewalls and molten pool, resulting in a correspondingly higher deposition rate.

3.2. Macroscopic morphology of SRA EGW and single-wire EGW

The macroscopic morphologies of the front weld, back weld, and weld seam for both SRA EGW and single-wire EGW (obtained using the welding parameters specified in TABLE 3) are presented in Fig. 5.

As shown in Figs. 5(a1), 5(a2), 5(b1), and 5(b2), the macroscopic morphologies of the weld seams differ significantly between the two EGW processes. From Figs. 5(a3) and 5(b3), it can be observed that the weld seams produced by SRA EGW and single-wire EGW are nearly symmetrical on both sides, with the former exhibiting superior symmetry. Additionally, the two welding processes differ in the morphology of the weld seam along the groove sidewalls. In the thickness direction (from the front to the back weld), the sidewall penetration of SRA EGW remains nearly constant initially, then increases sharply and reaches its maximum near the back weld. By contrast, the sidewall penetration of single-wire EGW stays relatively constant, with an increase occurring only near the back weld. Measurements indicate that both the minimum and maximum sidewall penetration values of single-wire EGW are smaller than those of SRA EGW. Further analysis reveals that although the sidewall penetration of single-wire EGW does not vary significantly, a slight increase is observed at approximately one-third of the plate thickness (near the front weld), with only a minor overall increase toward the back weld. In contrast, the sidewall penetration of SRA EGW shows a more pronounced increase at around one-third of the plate thickness (near the front weld).

The differences in sidewall weld seam morphology between the two EGW processes can be attributed to several factors. Both processes use a fixed, non-oscillating welding torch, positioned

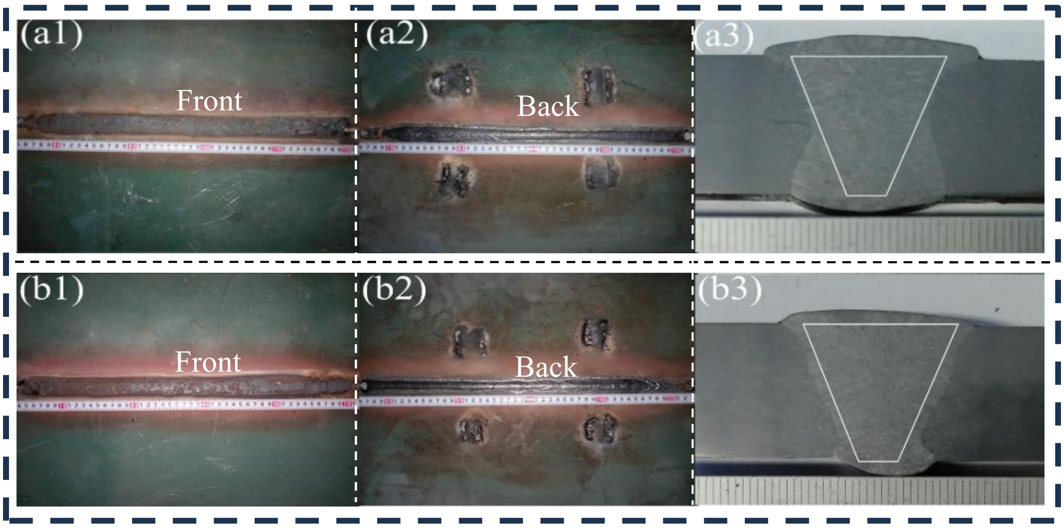

Fig. 5. Macroscopic morphology of welded joints between two EGW welding processes: (a1) Seven-wire front weld seam; (a2) Seven-wire back weld seam; (a3) Macroscopic morphology of seven-wire weld seam; (b1) Single-wire front weld seam; (b2) Single-wire back weld seam; (b3) Macroscopic morphology of single-wire weld seam

at one-third of the plate thickness and closer to the front weld (as illustrated in Fig. 1). For both EGW processes, sidewall penetration is primarily determined by heat transfer between the molten pool and the sidewall base metal. The SRA EGW process, with its shorter arc length, features a more direct heat transfer path from the arc to the molten pool, thereby reducing heat loss. Additionally, the rotating arc generates a strong stirring effect on the molten pool, which enhances heat transfer between the molten pool and the sidewall base metal and facilitates more efficient heat delivery to the sidewalls. In both welding processes, sidewall penetration increases along the thickness direction from the front to the back weld. This is attributed to the narrow groove gap, which allows the transferred heat to flow more easily toward the back weld – resulting in the maximum sidewall penetration occurring near the back weld.

3.3. Microstructure of SRA EGW and single-wire EGW

Figs. 6(a) and 6(b) depict the microstructures of weld seams fabricated via the SRA EGW process, whereas Figs. 6(d) and 6(e) illustrate those produced by the single-wire EGW process. Both weld seams are predominantly composed of ferrite, with only a small fraction of pearlite dispersed throughout.

In the SRA EGW weld seam, the ferrite phase consists of three distinct morphologies: relatively coarse proeutectoid ferrite (PF), acicular ferrite (AF), and fine-grained ferrite. Notably, the single-wire EGW weld seam exhibits an analogous phase composition, also containing coarse PF, AF, and fine-grained ferrite. Despite this similarity in phase constituents, the SRA EGW weld seam is distinguished by a more refined and homogeneous microstructure. This distinction can be attributed to two key factors associated with the SRA EGW process: a higher welding speed, which results in a significantly lower heat input compared to the single-wire EGW process; the self-rotating behavior of the welding arc, which not only enhances heat transfer efficiency (leading to a higher cooling rate) but also induces intense stirring in the molten pool. This stirring effect directly contributes to grain refinement and a more uniform distribution of microstructural phases [15].

Additionally, the reduced exposure time to high temperatures during SRA EGW further promotes the nucleation and growth of AF. Consequently, the SRA EGW weld seam exhibits a substantially higher volume fraction of AF than its single-wire counterpart – a difference that is closely correlated with improved impact toughness of the welded joint.

Figs. 6(c) and 6(f) provide insights into the microstructures of the FL regions for the two welding processes. In both cases, the FL – demarcating the boundary between the weld zone (WZ) and the HAZ – is clearly defined. However, the SRA EGW process, due to its more uniform and rapid heat transfer characteristics, yields a finer-grained microstructure in the HAZ compared to the single-wire EGW process.

Microstructurally, the HAZ of the SRA EGW process is predominantly composed of coarse PF. In contrast, the HAZ of the single-wire EGW process contains not only coarse PF but also side-plate ferrite. Importantly, both PF and side-plate ferrite are inherently brittle phases; their presence in the HAZ thus leads to a notable reduction in impact toughness for welded joints fabricated by either process [16].

Figs. 7(a1), 7(a2), 7(a3) and 7(b1), 7(b2), 7(b3) display the EBSD result of the weld seam produced by the SRA EGW and single-wire EGW processes. In the weld seam, typical intragranular AF morphology is observed, with fine inclusions

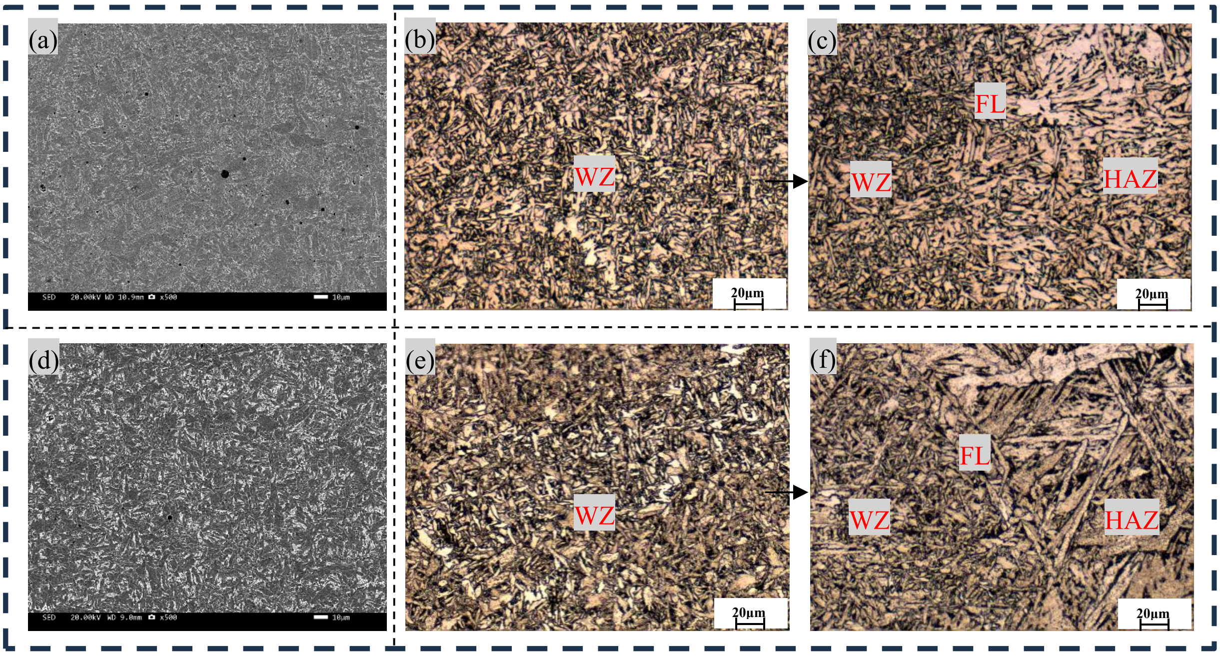

Fig. 6. SEM and OM comparison of welded joint between SRA EGW and single-wire EGW: (a) SEM of weld seam microstructure in SRA EGW, (b) OM of weld seam microstructure in SRA EGW, (c) FL microstructurein SRA EGW, (d) SEM of weld seam microstructure in single-wire EGW, (e) OM of weld seam microstructure in single-wire EGW, (f) FL microstructurein single-wire EGW

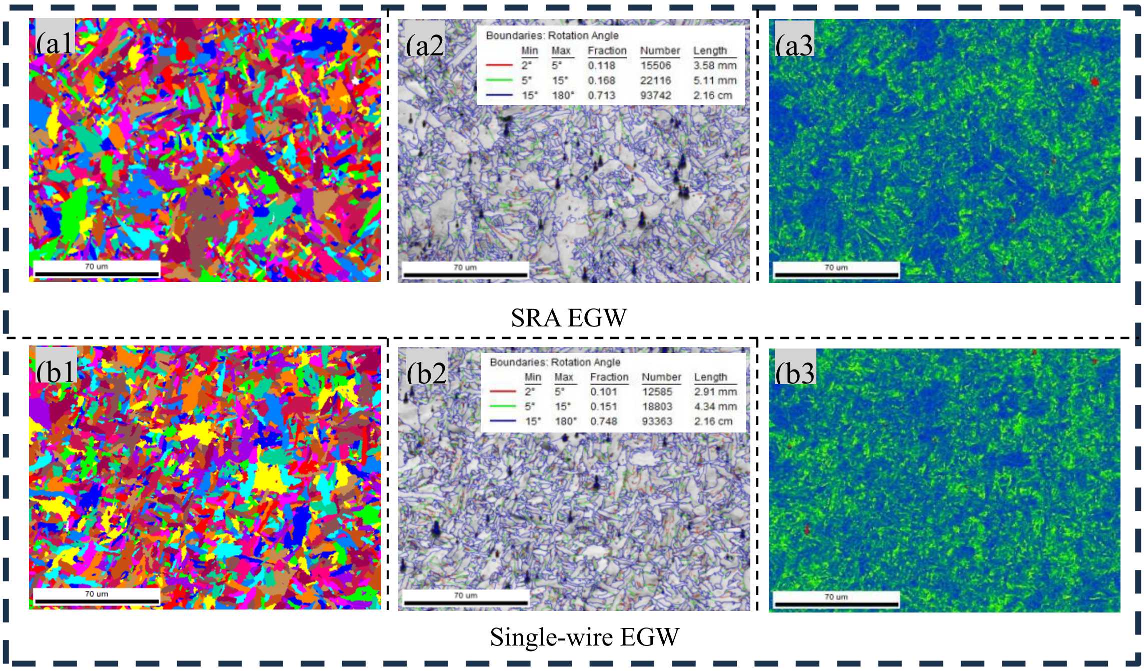

Boundaries: Rotation Angle

	Min	Max	Fraction	Number	Length
🟥	2°	5°	0.118	15506	3.58 mm
🟩	5°	15°	0.168	22116	5.11 mm
🟦	15°	180°	0.713	93742	2.16 cm

Boundaries: Rotation Angle

	Min	Max	Fraction	Number	Length
🟥	2°	5°	0.101	12585	2.91 mm
🟩	5°	15°	0.151	18803	4.34 mm
🟦	15°	180°	0.748	93363	2.16 cm

Fig. 7. EBSD comparison of welded joint between SRA EGW and single-wire EGW

acting as nucleation sites. Within the original austenite grains, numerous fine, interlaced AF structures form in a cross-like pattern. These fine AF structures precipitate radially around the inclusions, which function as nucleation centers [17].

When examining the grain orientation maps in 7(a1) and 7(b1), the grain orientations of the weld seams from both welding processes exhibit a diverse color distribution, which reflects complex crystallographic characteristics. Nevertheless, there are disparities in the specific color combinations and regional morphologies.

As for the grain boundary distribution data in 7(a2) and 7(b2), in the SRA EGW weld seam, the proportion of large angle grain boundaries (with a rotation angle ranging from 15° to 180°) is 0.713, and the proportion of small angle grain boundaries (with a rotation angle in the range of 2° to 5° accounting for 0.118, and 5° to 15° accounting for 0.169) is more advantageous. In contrast, for the single-wire EGW weld seam, the proportion of large angle grain boundaries (rotation angle 15° to 180°) is 0.749, and the proportion of small angle grain boundaries (rotation angle 2° to 5° accounting for 0.151, and 5° to 15° accounting for 0.101) is relatively lower. Since small angle grain boundaries possess low energy and strong bonding ability, which positively impacts the plasticity and toughness of the material, this suggests that the SRA EGW weld seam may have greater advantages in terms of mechanical properties.

Additionally, from 7(a3) and 7(b3), it can also be observed that the microstructure morphology in the SRA EGW weld seam area is superior in terms of distribution uniformity compared to that in the single -wire EGW weld seam, further highlighting the advantages of the weld microstructure under the SRA EGW process. These advantages, along with factors such as grain boundary distribution, jointly influence the performance of the weld.

3.4. Mechanical properties of SRA EGW and single-wire EGW

Microhardness testing was conducted on the welded joints from the two EGW processes using the Vickers hardness method, and the results are presented in Fig. 8(a). In both processes, the hardness values of the WZ and HAZ are higher than those of the BM. However, the hardness values in the WZ and HAZ of the SRA EGW are slightly lower than those of the single-wire EGW process. During the single-wire EGW process, the rapid cooling rate leads to a short high-temperature residence time and fast cooling in the HAZ, particularly in the coarse-grained heat-affected zone (CGHAZ). As a result, grains tend to undergo "rapid growth" without sufficient time for refinement, ultimately forming coarse ferrite interspersed with a small amount of pearlite. In contrast, during the SRA EGW process, the stirring effect of the rotating arc enhances molten pool convection, which flattens the temperature gradient in the HAZ and facilitates more thorough grain refinement (EBSD analysis confirms a higher proportion of low-angle grain boundaries, as shown in Fig. 7). Although the fine-grained structure achieves enhanced strength through grain refinement strengthening, its hardness is lower than that of the coarse-grained hard-phase structure formed in single-wire EGW. Further analysis shows that the hardness values near the backside of the weld are higher than those near the front side. This is because the weld regions near the backside are mainly formed through thermal transfer from the molten pool, leading to lower heat input and faster cooling rates. As a result, the microstructure is refined, causing an increase in hardness.

Transverse tensile tests were carried out on the welded joints from both EGW processes, and longitudinal tensile tests were performed on the welds. The results are displayed in Fig. 8(b). As seen from Fig. 8(b), the fracture location in the transverse tensile tests for both welding processes is in the BM, which indicates that the tensile strength of the WZ is higher than that of the BM. Specifically, the average tensile strength of the welded joints produced by the single-wire EGW is 540 MPa (average values), while that for the SRA EGW is 561 MPa (average value). The average tensile strength of the WZ in the single-wire EGW is 589 MPa (average value), and the corresponding value in the SRA EGW is 600 MPa (average value).

Charpy impact tests were conducted on welds fabricated via both EGW processes at a temperature of –20°C, with three replicate samples tested for each process; the results are presented in Fig. 9(a). The tests revealed that the average impact energy of the SRA EGW welds reached 78 J, whereas the corresponding value for the single-wire EGW welds was 72 J. When combined with the microstructural characteristics of the two weld proceseses, this difference in impact energy can be attributed to phase composition: although both welds exhibit relatively fine microstructures, the SRA EGW welds contain a higher proportion of AF compared to the single-wire EGW welds. This elevated AF content directly contributes to the superior low-temperature impact toughness observed in the SRA EGW welds.

To further elucidate the mechanisms underlying the toughness discrepancy between the two processes, SEM was employed to analyze the fracture surfaces of the impact test specimens, with the results shown in Figs. 9(b) and 9(c). Both fracture surfaces exhibit typical ductile fracture features characterized by dimple morphology – numerous dimple-shaped depressions are visible, with inclusions distributed at the bottom of these dimples. However, distinct differences emerge between the two: the fracture surface of the SRA EGW welds contains a greater number of deeper dimples, whereas the single-wire EGW weld fracture surface, while still dominated by dimples, displays occasional quasi-cleavage planes.

Overall, ductile dimples constitute the primary microstructural feature on the impact fracture surfaces of both EGW weld zones, which serves as a key factor underpinning their favorable toughness. The higher density and greater depth of dimples in the SRA EGW welds further corroborate its superior

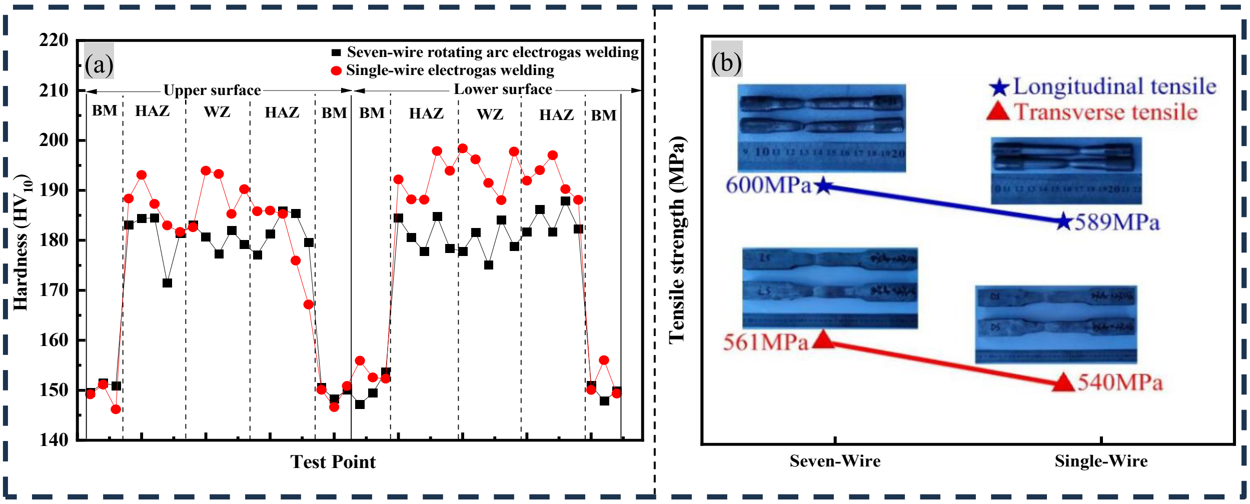

Fig. 8. Microhardness and tensile strength of welded joints between SRA EGW and single-wire EGW

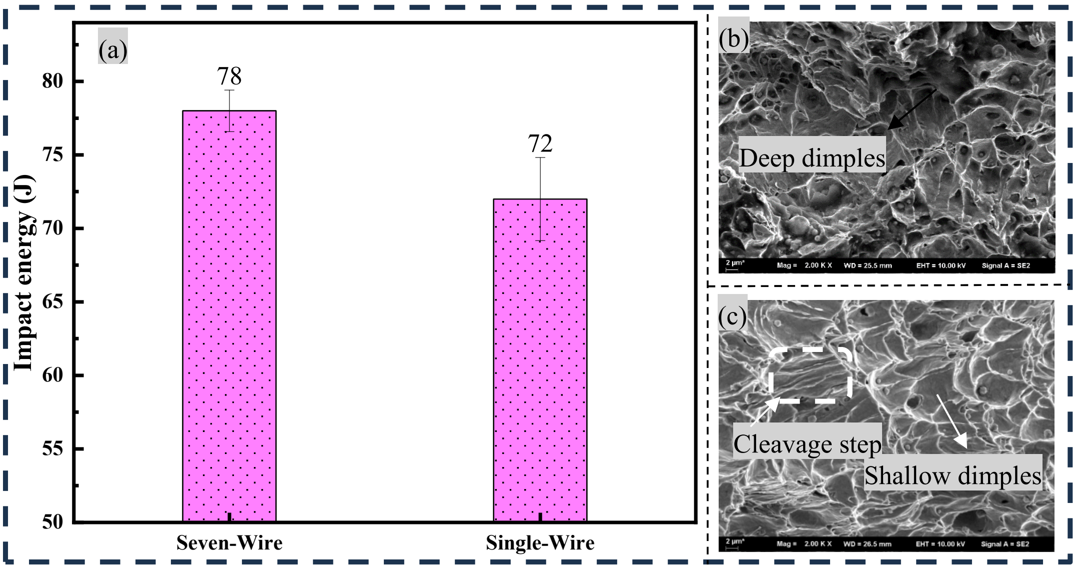

Fig. 9. Impact result of welded joints between SRA EGW and single-wire EGW

impact performance, which is consistent with the earlier impact energy test results.

4. Conclusions

(1) Under identical welding conditions, the average welding speed, deposition rate, wire melting rate, and deposition efficiency of SRA EGW are 6.6 cm/min, 137.3 g/min, 138.9 g/min, and 98.9%, respectively. For single-wire EGW, the corresponding values are 5.5 cm/min, 128.2 g/min, 133.8 g/min, and 95.8%, respectively. Compared to single-wire EGW, the average welding speed, wire melting rate, and resistance heat of wire extension of SRA EGW are increased by approximately 20%, 4%, and 38%, respectively. The higher wire melting rate of SRA EGW relative to single-wire EGW can be attributed to its greater resistance heat. Additionally, the relatively enclosed welding environment of both EGW processes enables most of the generated spatter to be retained on the groove sidewalls and within the molten pool, resulting in a correspondingly higher deposition efficiency.

(2) The average tensile strength of the welded joints produced by the single-wire EGW is 540 MPa, while that for the SRA EGW is 561 MPa. The average tensile strength of the WZ in the single-wire EGW is 589 MPa, and the corresponding value in the SRA EGW is 600 MPa.The tests revealed that the average impact energy of the SRA EGW welds reached 78 J, whereas the corresponding value for the single-wire EGW welds was 72 J. The difference can be attributed to phase composition: although both welds exhibit relatively fine microstructures, the SRA EGW welds contain a higher proportion of AF compared to the single-wire EGW welds.

Declaration of Competing Interest

The authors declare that they have no known competing financial interests or personal relationships that could have appeared to influence the work reported in this paper.

Acknowdgement

This research was funded by the Jiangsu Province in “333 Talents Project”; the Jiangsu Province Industrial Perception and Intelligent Manufacturing Equipment Engineering Research Center (Grant No. 2025).

REFERENCE

[1] S. Yang, L. Ju, W. Cong, On the Heterogeneous Microstructure Development in the Welded Joint of 12MnNiVR Pressure Vessel Steel Subjected to High Heat Input Electrogas Welding. J. Mater. Sci. Technol. **35** (8), 235-240 (2019).

[2] K. Seo, H. Ryoo, H.J. Kim, Characterization of the Local Brittle Layer formed in Electro-gas Weld Metals. Weld. World. **65**, 513-514 (2020).

[3] K. Seo, H. Ryoo, H.J. Kim, Local Variation of Impact Toughness in Tandem Electro-gas Welded Joint. Weld. World. **64** (3), 457-465 (2020).

[4] T.Q. Tang, J. Li, K. Liu, Effect of Ti on Microstructure and Mechanical Properties of Vertical EGW Welded Joint of 12MnniVr steel. Arch. Metall. Mater. **70** (2), 785-796 (2025).

[5] J. Fu, Q. Tao, X.A. Yang, The Effect of Heat Source Path on Thermal Evolution during Electro-gas Welding of Thick Steel Plates. Materials. **15** (6), 2215 (2022).

[6] Y. Chen, C.F. Fang, T. Zhang, Q.T. Li, Q. Hong, L. Hua, The Decoupling Behavior of Arc Coupling and Rotating in Seven-wire Rotating Arc EGW. J. Manuf. Process. **55**, 96-102 (2020).

[7] Y. Chen, C.F. Fang, Z.D. Yang, J.Y. Wang, G.X. Xu, X.Y. Gu, Cable-type Welding Wire Arc Welding. Int. J. Adv. Manuf. Tech. **94**, 835-844 (2018).

[8] Y. Chen, C.F. Fang, Z.D. Yang, J.Y. Wang, M.F. Wu, K. Qi, Cable-type welding wire submerged arc surfacing. J. Mater. Process. Tech. **249**, 25-31 (2017).

[9] Z.Q. Wang, Y. Shi, Z.X. Zhang, L.J. Zhang, J.M. Wang, K.H. Huang, X.D. Chen, X.R. Wang, P. He, In Situ Synthesis of Carbide Reinforced Fe-Cu-Ni-Mo-Ti High Entropy Alloy Coatings using GTAW Cladding with Cable-type Welding Wire. Mater. Lett. **324**, 132706 (2022).

[10] Z.D. Yang, J.D. Huang, K. Xu, P. He, Effect of Polarities and Shielding Gases in CWW GMAW. Mater. Manuf. Process. **39** (2), 227-236 (2024).

[11] K. Xu, P.B. Wu, X.M. Liang, J. Chen, R.S. Huang, Analysis of Characteristics of Aluminum Alloy Laser Multi Stranded Welding Wire MIG Hybrid Welding. Transit. China. Weld. I. **42** (1), 16-23 (2021).

[12] Y. Chen, C.F. Fang, Q.T. Li, T. Zhang, J.X. Li, F. Gao, Droplet Formation and Motion Characteristics in Seven-wire Rotating Arc Electrogas Welding. Int. J. Adv. Manuf. Tech. **107**, 3363-3369 (2020).

[13] Y. Chen, T. Zhang, B.Y. Li, H. Dong, C.F. Fang, R.Y. Sun, Temperature Field and Flow Field of Molten Pool in SRA EGW. Integr. Ferroelectr. **240** (2), 398-406 (2024).

[14] Y. Chen, X.S. Sun, T. Zhang, Q.T. Li, S.Y. Ni, C.F. Fang, Arc Rotating Behavior of SRA EGW in AH36 Steel. Mater. Manuf. Process. **35** (5), 556-563 (2020).

[15] Y. Chen, C.F. Fang, Z.D. Yang, J.Y. Wang, M.F. Wu, S.J. Chen, A Study on Sidewall Penetration of Cable-type Welding Wire Electrogas Welding. Weld. World. **61**, 979-986 (2017).

[16] C.F. Ma, X.L. Wang, Z.X. Ni, Z.H. Chen, Z.D. Yang, Effect of post-weld heat treatment on the microstructure and mechanical properties of CWW GMAW. Mod. Phys. Lett. B. **39** (6), 2442013 (2025).

[17] Y. Chen, Y.L. Xu, X.R. Zhao, Y.F. Wang, W.W. Yu, T. Zhang, C.F. Fang. Microstructure and Mechanical Properties of Toughened Seven-Wire Electrogas Welding. Materials **18** (7), 1581 (2025).